nature communications

Article

https://doi.org/10.1038/s41467-024-53858-2

Constructing organoid-brain-computer interfaces for neurofunctional repair after brain injury

Received: 6 June 2024

Accepted: 24 October 2024

Published online: 06 November 2024

Check for updates

Nan Hu[1,2,4], Jian-Xin Shi[1,2,4], Chong Chen[1,2,3,4], Hai-Huan Xu[1,2,3], Zhe-Han Chang[1,2], Peng-Fei Hu[1,2], Di Guo[1,2], Xiao-Wang Zhang[1,2], Wen-Wei Shao[1,2], Xiu Fan[1,2], Jia-Chen Zuo[1,2], Dong Ming[1,2] & Xiao-Hong Li[1,2,5]

The reconstruction of damaged neural circuits is critical for neurological repair after brain injury. Classical brain-computer interfaces (BCIs) allow direct communication between the brain and external controllers to compensate for lost functions. Importantly, there is increasing potential for generalized BCIs to input information into the brains to restore damage, but their effectiveness is limited when a large injured cavity is caused. Notably, it might be overcome by transplantation of brain organoids into the damaged region. Here, we construct innovative BCIs mediated by implantable organoids, coined as organoid-brain-computer interfaces (OBCIs). We assess the prolonged safety and feasibility of the OBCIs, and explore neuroregulatory strategies. OBCI stimulation promotes progressive differentiation of grafts and enhances structural-functional connections within organoids and the host brain, promising to repair the damaged brain via regenerating and regulating, potentially directing neurons to preselected targets and recovering functional neural networks in the future.

Brain injury imposes a significant socio-economic burden and severely impacts the life quality of patients[1]. Surgery, medication, and rehabilitation are often limited in recovering damaged function[2]. Classical brain-computer interfaces (BCIs) allowing direct communication between the brain and external computers, permit users to spell words, move cursors, and control wheelchairs or robotic arms[3,4]. Notably, there is growing potential for developing BCIs that input information into the brain, such as deep brain stimulation (DBS) or transcranial electrical stimulation (TES), to modulate brain injury[5]. Neural interface (electrodes) used for signal recording and stimulation, is critical in BCIs. Electrical stimulation via neural interfaces has been reported to promote differentiation or maturation of neural stem cells (NSCs)[6], and to modulate the plasticity of the neural tissue[7], further regenerating injured brain tissue[8,9]. Brain injury results in massive loss of neural cells, particularly when large cavities are formed[5,10], which limits implantable electrodes to work well without healthy cell replacement. Thus, it is necessary to construct innovative BCIs mediated by replaced cells to repair brain injury.

Brain organoids, a three-dimensional (3D) neural tissue cultured in vitro, can simulate neurogenesis, neuronal migration, cortical stratification, and neural circuits of the human brain[11–13]. When implanted into the sensory[14], motor[15], and visual cortices of a host[16,17], organoid displayed robust survival, progressive differentiation, and extensive axonal growth towards the host brain[18–20], thereby partly participating in the neural activities of the host. However, there are still non-negligible problems with organoid transplantation. Immature organoids, which contain massive ventricular zone (VZ) cells, may pose risks of overgrowth in the host brain[19]. Furthermore, the efferent

[1]Academy of Medical Engineering and Translational Medicine, Tianjin University, Tianjin, China. [2]Haihe Laboratory of Brain-Computer Interaction and Human–Machine Integration, Tianjin, China. [3]Tianjin Key Laboratory of Neurotrauma Repair, Characteristic Medical Center of People's Armed Police Forces, Tianjin, China. [4]These authors contributed equally: Nan Hu, Jian-Xin Shi, Chong Chen. [5]These authors jointly supervised this work: Xiao-Hong-Li. e-mail: xhli18@tju.edu.cn

projects from the grafts into the host brain were spontaneous without anatomical targets, restricting the reconstruction of targeted neural circuits between grafts and hosts. Considering that neural stimulation could facilitate neural differentiation and guide cell migration and axon elongation direction[21,22], it is reasonable to hypothesize that stimulation in vivo may enhance the development of transplanted organoids and promote their projections to host brain, ultimately aiming to restore functional neural networks.

BCIs and organoid transplantation are two distinct strategies to restore neurological function. Research has indicated that delivering electrical stimulation to transplanted cells can promote cell regeneration and axonal sprouting in situ[23,24]. Additionally, stimulation enhanced the plasticity of neurons surrounding damaged areas and guided the targeted migration of transplanted cells[7,25,22]. An implantable electrical–cellular hybrid device was first introduced by Stieglitz et al.[26], which has been proven to promote functional cellular integration with brain tissue, enhance synaptic connections within grafts and existing neural circuitry, and reduce scar tissue formation[27,28]. Furthermore, Byeongtaek et al. developed a conductive polymer system for the delivery of NSCs and electrical modulation, demonstrating that stimulation of NSC transplants improved brain recovery following a stroke more than electrical regulation or NSC transplant therapy alone[29]. However, organoid-brain-computer interfaces (OBCIs)—implantable neural interfaces with organoids that integrate into the host tissue—remain a largely unexplored concept despite offering innovative treatment opportunities.

In recent years, rigid electrodes have been implanted into transplanted organoids to acutely detect the electrical activity of grafts or host brains to assess the neural connectivity between the grafts and the host brain[16–18]. However, the modulation of graft development through the implantable neural interfaces remains largely unexplored. Notably, flexible electrodes, which possess appropriate mechanical properties and excellent biocompatibility, outperform rigid electrodes in maintaining the prolonged quality of recorded neural signals and in establishing stable electrode-neuron interfaces[30–32]. Therefore, we construct innovative OBCIs that combine the merits of transplanted organoids with neural regulation to repair brain injury. First, we assess the prolonged security and feasibility of the OBCI system and explore schemes for regulating organoid grafts. Progressive differentiation and maturation of the grafts are enhanced after early-stage regulation. Additionally, structural-functional connections are developed between the grafts and the host brain after late-stage regulation, displaying increased synaptic junctions and ultimately promoting the repair of damaged functions of the host. In the future, OBCIs can be integrated with closed-loop systems to create a bidirectional BCI framework, which has the potential to reconstruct specific neural functional circuits within the host brain.

Results

An organoid-electrode complex in vitro was created to simulate an organoid brain-computer interface in vivo

To explore appropriate parameters for regulating OBCIs, we constructed an organoid-electrode complex in vitro to mimic OBCI (Fig. 1A, B). The organoids, cultured for 90 days in vitro, were immobilized onto a 3D-printed scaffold to ensure their stability during the electrode implantation, recording, and stimulation phases (Supplementary Fig. 1A, B). Subsequently, dual-shank flexible electrodes were inserted into the organoids (Supplementary Fig. 1C–E). After one month, enriched $NeuN^+$ cells, cortical plates expressing cortical layers VI (TBR1), V (CTIP2), and III (SATB2) from deep to superficial layers, neuronal markers SMI312 and MAP2 were observed in the day 120 (D120) organoids (Supplementary Fig. 1G–I). In addition, astrocytes (GFAP), and glutamatergic neurons marked by vesicular glutamate transporter 1 (VGLUT1), were found in the organoids (Supplementary Fig. 1J, K). The synaptic structures, characterized by the presynaptic marker synapsin (SYN) and post-synaptic structures (PSD95), demonstrated that abundant synapses formed within the organoids at D120 (Supplementary Fig. 1L, M). Furthermore, longitudinal functional monitoring of the organoids showed gradual functional maturation of them from D90 to D150, characterized by an increase in spike firing and burst activity over time (Supplementary Fig. 1N). The raster plots revealed a transition from sparse, isolated activity to burst activity between D90 and D150 (Supplementary Fig. 1O). Increased spike firing rate, burst number, and burst duration indicated the electrophysiological maturation of the organoid over time (Supplementary Fig. 1P–R).

Neuroregulatory strategy targeting brain organoids was explored in vitro

To investigate effective stimulated parameters, we selected three electrode sites evenly distributed along a shank in the organoid-electrodes complex, in which we conducted experiments to assess frequency and amplitude gradients. Specifically, we tested six frequency-gradient values ranging from 1 Hz to 100 Hz (1, 10, 30, 50, 70, and 100 Hz) and 4 gradient amplitudes ranging from 10 μA to 70 μA (10, 30, 50, and 70 μA). Our results revealed that organoids exhibited a higher firing frequency when subjected to a constant-current, cathode-leading, biphasic square waveform at 50 Hz and 50 μA (Fig. 1C, Supplementary Fig. 1F). A shorter interspike interval (ISI) was observed following electrical stimulation (ES) compared to the non-stimulated organoids (Fig. 1D, E). To validate the effect of ES on the differentiation of organoids, we examined the laminar architecture of the cortical plate within the organoids (Fig. 1F). The results indicated a reduced expression of TBR1 and an increased proportion of CTIP2 in the ES group compared to the controls, while there was no significant difference in SATB2 expression between the two groups (Fig. 1G). We then found more abundant synapses in the ES group than in the controls (Fig. 1H, I). Additionally, the VGLUT1 expression was higher in the ES group (Fig. 1J, K), whereas the number of astrocytes decreased in the ES group compared to the controls (Fig. 1L, M). Furthermore, we assessed their electrophysiological properties. Higher spike firing rate, increased network synchrony, and greater overall low-frequency energy were found in the ES group than in the controls, which indicated that ES promoted the functional maturation of the organoids (Fig. 1N–R).

The organoid-brain-computer interface was constructed and maintained effectively for several months

Damaged cavities were created in the primary sensory cortex (S1) of the host to simulate cortical injury. Distinct cavities and immune response of the injured site were found at 1 week, 1 month, and 2 months post-injury (Supplementary Fig. 2A–C). Statistical analysis revealed that the number of microglia aggregated at the injured sites decreased from 1 week to 2 months post-injury, while the number of astrocytes remained relatively stable over time (Supplementary Fig. 2D–F). Subsequently, a BCI mediated by transplanted organoids was developed to facilitate brain repair. GFP^+ organoids cultured for 40 days in vitro were transplanted into the S1 of the host, which was defined as 0 days post-transplantation (0 dpt). A secondary craniotomy was performed at 25 dpt to implant a dual-shank flexible electrode into the organoid or the host brain for signal recording and stimulation. With the assistance of ultraviolet (UV) light, one shank was inserted into the organoid located in the S1, and the other shank was implanted into the adjacent primary motor cortex (M1) of the host, which was coined as OBCI system (Fig. 2A–C).

To evaluate the security of OBCI to tissues in vivo, immunostaining was conducted around the electrodes in both the grafts and host brain at 60 and 120 dpt (Fig. 2C, D). No aggregation of microglia ($IBA1^+$) or astrocytes ($GFAP^+$) was observed around the electrodes (Fig. 2C-a, C-b, D-a, D-b). A homeostatic microglial marker ($P2RY12^+$)

https://doi.org/10.1038/s41467-024-53858-2

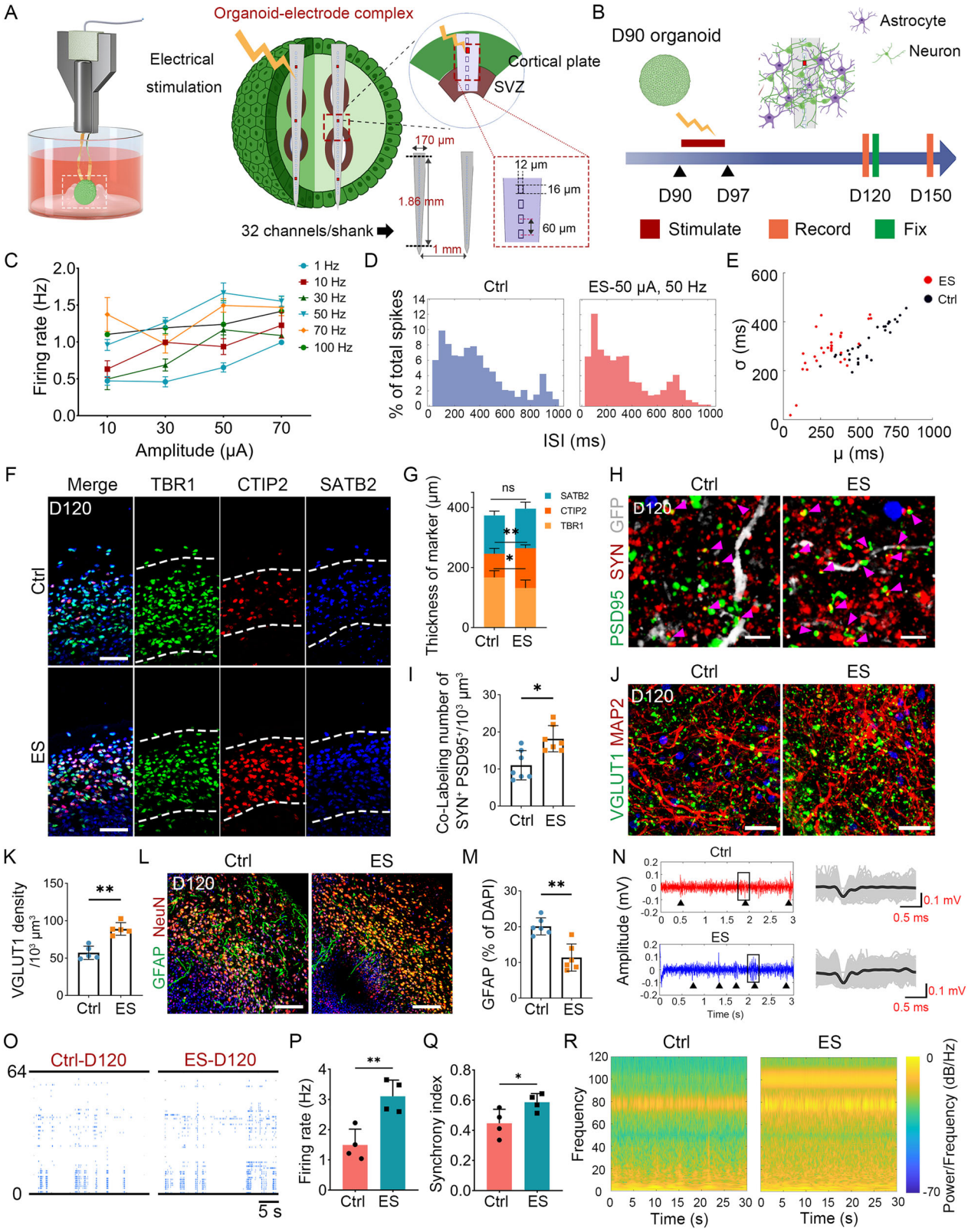

and an oxidative stress marker (iNOS$^+$) were detected, indicating that the majority of the microglia remained unactivated (Fig. 2C-c, C-d). In the host brain, vascular structures were distributed around the electrodes, and neurons exhibited abundant synapsin expression (Fig. 2D-c, D-d). In the grafts, progressive differentiation (DCX) and maturation (MAP2) occurred in vivo, accompanied by vascular infiltration (Fig. 2E–G). Furthermore, SYN$^+$ and PSD95$^+$ colocalized puncta suggested synaptic connectivity within the grafts (Fig. 2H). Collectively, the inserted electrodes did not induce damage to either the organoid or the host brain. Notably, regarding the prolonged monitoring, we found an increase in signal activity over time, characterized by active high-frequency spikes and low-frequency energy, reflecting the maturation of the brain organoids and the sustained efficacy of the electrodes (Fig. 2I, J). For host safety, approximately 85% of grafted

Fig. 1 | The stimulated parameter was explored based on the organoid-electrode complex. A Schematic illustrating the organoid-electrode complex (brain organoid and dual-shank flexible electrodes). The red squares represent the stimulated sites. The red dotted square on the right shows the details of electrode parameters. SVZ, subventricular zone; (**B**) Schematic illustration of the timeline of regulating, fixating, and recording; (**C**) The firing rate is a function of amplitude or frequency for all stimulation frequencies, n = 3 organoids; (**D**) Histogram plots of inter-spike intervals (ISIs) pre- and post-stimulus are shown from organoid in vitro; (**E**) σ is plotted as a function of μ across all channels for organoid pre- and post-stimulus; (**F**) Markers for laminar structure of organoids for SATB2 (blue), CTIP2 (red), TBR1(green) at D120 in the Ctrl and ES group. Scale bar: 50 μm; (**G**) The quantification of $TBR1^+$, $CTIP^+$, and $SATB2^+$ cells at D120 in different groups, n = 6 organoids; (**H**) Immunostaining for SYN (red) and PSD95 (green) is displayed at D120. Scale bar: 10 μm; (**I**) Co-labeling number of SYN^+ $PSD95^+$ puncta are quantified, n = 7 organoids, $^*P < 0.05$; (**J**) VGLUT1 and MAP2 are shown at D120. Scale bar: 30 μm; (**K**) Quantification of VGLUT1 puncta are shown, n = 5 organoids, $^{**}P < 0.01$; (**L**) Immunostaining for astrocyte (GFAP, green) and NeuN (red) is shown at D120. Scale bar: 100 μm; (**M**) Quantitative data of the expression of GFAP, n = 6 organoids, $^{**}P < 0.01$; (**N**) High-pass trace of a representative 3-second recording (left) and detected spike waveform (right) in the two groups at D120; (**O**) Raster plot in the ES (bottom) and Ctrl group (top) at D120; (**P**, **Q**) Quantification of firing rate and synchrony index in the ES and Ctrl group at D120, n = 4 organoids, $^*P < 0.05$, $^{**}P < 0.01$; (**R**) Spectrograms were derived from the entire electrodes in the ES and Ctrl group (left) at D120. Mean ± SD is shown for each condition. Statistical significance was tested with an unpaired two-tailed t-test for two-group comparisons. **A**, **B** was created with BioRender.com (BioRender.com/y26f932) released under a CC-BY 4.0 International license.

animals survived beyond 180 days, showing no significant differences among the BO, BO-ET, and BO-ET-ES groups (Fig. 2K). For long-term stability of signals, the signal-to-noise ratio (SNR) of flexible electrodes was assessed in vivo, which decreased at 180 dpt compared to 60 dpt, but remained above 10 dB (Fig. 2L).

Early-stage stimulation promoted neurodevelopment via the organoid-brain-computer interface

Two critical time points about survival (30 dpt) and integration (60 dpt) were selected to regulate grafts according to the developmental status of transplanted organoids. For early-stage stimulation, the parameters of stimulation were confirmed in the organoid-electrode complex in vitro. Given that prolonged stimulation for more than 10 days decreased neuronal activity (Supplementary Fig. 3A–E), we regulated the grafts for a duration of 10 days in vivo (Fig. 3A). Regarding the safety of OBCI under stimulation, infiltrated microglia and astrocytes were detected. There were no significant differences in microglia within the grafts at 60 dpt among the three groups, nor from 60 to 180 dpt in the BO-ET-ES group (Supplementary Fig. 4A–D). For astrocytes, $GFAP^+$ cells were scattered throughout the grafts, with a decrease in the BO-ET-ES group at 120 dpt, compared to the BO and BO-ET groups (Supplementary Fig. 4E, F), while the number of astrocytes increased from 60 dpt to 180 dpt with a significant difference in the BO-ET-ES group (Supplementary Fig. 4G–H). To evaluate whether activated immune response within grafts, we stained for the IBA1, P2RY12, and iNOS. Results showed that over 90% of $P2RY12^+$ cells co-labeled with $IBA1^+$ cells, while only about 2% of $iNOS^+$ cells co-labeled with $IBA1^+$ cells (Supplementary Fig. 4I–L). Few inflammatory factors (IL-1β and TNF-α) were detected surrounding the electrodes at 60 and 180 dpt (Supplementary Fig. 4M, N). Collectively, no activated immune response occurred within grafts under stimulation.

To assess whether early-stage stimulation can enhance the neurodevelopment of organoids, we evaluated their survival potential following regulation (Fig. 3A). Our findings indicated that graft volumes increased after stimulation at 60 dpt, reaching statistical significance (Fig. 3B, C). Given the larger graft volume observed in BO-ET-ES group, we examined the expression of proliferating cells ($Ki67^+$) at 60, 120, and 180 dpt. The ratio of $Ki67^+$ cells were higher at 60 dpt in the BO-ET-ES group than that in the BO and BO-ET groups (Fig. 3D, E), while the proportion of Ki67-labeled cells decreased significantly in the BO-ET-ES group over time, indicating no sustained proliferation within grafts (Supplementary Fig. 5A–D). And a few phosphor-vimentin (p-VIM) that analyze symmetric/asymmetric cell division patterns, was detected (Supplementary Fig. 5E, F). Notably, no $OCT4^+$ or $SSEA4^+$ cells were detected among the HN^+ cells at 60, 120, and 180 dpt (Supplementary Fig. 5G–J). No tumors or teratomas were detected in any subject.

Next, we detected the endothelial cells marker (CD31) (Fig. 3F), demonstrating more vascular infiltration into the transplanted organoids in the BO-ET-ES group with a tubular morphology (Fig. 3G). In addition, decreased neural progenitor cells ($PAX6^+$) and increased mature neurons ($NeuN^+$) were found in the BO-ET-ES group compared to the BO and BO-ET group, suggesting progressive differentiation of grafts at 120 dpt (Fig. 3H–K). Furthermore, the subclass of cortical neurons (SATB2 and CTIP2) in engrafted organoids increased in the BO-ET-ES group compared with the BO or BO-ET group (Fig. 3L–O). Specially, to determine the long-term survival and differentiation of grafts in the BO-ET-ES group, we longitudinally tracked the viability of organoid grafts from 60 dpt to 180 dpt in vivo (Supplementary Fig. 6A, B). Increasing growth with no obvious apoptotic cells ($TUNEL^+$) within grafts were found in the BO-ET-ES group, which may be supported by nutrient supply from more infiltrated vascular (Supplementary Fig. 6C–F). Additionally, decreased $PAX6^+$ cells and increased $NeuN^+$ cells were also observed with statistical significance from 60 dpt to 180 dpt in the BO-ET-ES group (Supplementary Fig. 6G–J). The expression of CTIP2 and SATB2 was higher in BO-ET-ES group at 180 dpt, compared to 60 dpt (Supplementary Fig. 6K–N). For 180 dpt, immunostaining for the graft-derived presynaptic marker human synaptophysin (hSYN) and the PSD95 showed multiple colocalized puncta of hSYN and PSD95, suggesting more synaptic connectivity in the BO-ET-ES groups, compared to the BO and BO-ET groups.

Early-stage stimulation facilitated the functional maturation of grafts via the organoid-brain-computer interface

Having documented the progressive maturation of the organoid by histology, we next evaluated the functional maturation of grafts using OBCIs (Fig. 4A, B). During the 10-day stimulation period, the firing rate of the BO-ET-ES group improved significantly compared to the BO-ET group (Fig. 4C), while the amplitude increased without a significant difference compared to the controls (Supplementary Fig. 7A). In the local field potential (LFP) analysis, we observed that the energy in the low-frequency band remained stable, as well as the information entropy, while the energy of the middle and high-frequency bands in the BO-ET-ES group increased significantly compared to the BO-ET group (Fig. 4D, Supplementary Fig. 7B–F). Given that electrical stimulation promoted progressive maturation of the engrafted organoids, we monitored the long-term electrophysiological activity of the grafts from 40 to 180 dpt to explore whether it correlated with functional maturity (Fig. 4E, F). The firing rate, burst number, and burst duration of the BO-ET-ES group continued to increase, demonstrating a significant difference from the BO-ET group, while the spike amplitude stabilized (Fig. 4G–J). In terms of LFP analysis, the Gamma-band energy in the BO-ET-ES group was higher than that in the BO-ET group, while it was not apparent in other bands (Fig. 4K–M, Supplementary Fig. 7G–J). In addition, cross-frequency phase-amplitude coupling (PAC), is an oscillatory dynamic, where the phase of low-frequency signals modulates the high-frequency signals. To investigate the neural networks of the engrafted organoids and the connectivity between the grafts and the host, we calculated the PAC of low-frequency and high-frequency signals of organoid grafts (Fig. 4N). Our results indicated

https://doi.org/10.1038/s41467-024-53858-2

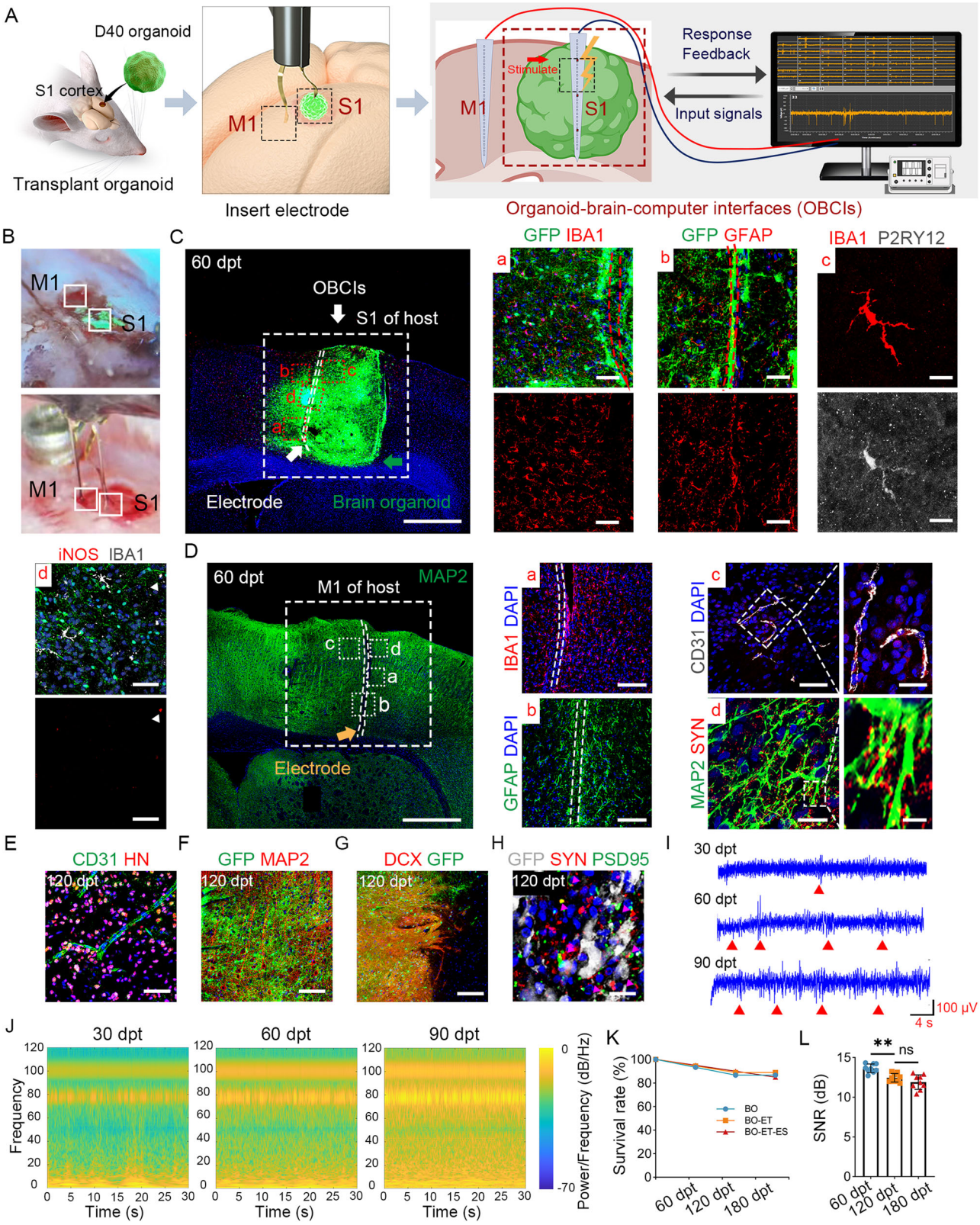

that the BO-ET-ES group exhibited significantly stronger PAC, suggesting enhanced functional maturity of the transplanted organoids (Fig. 4O).

To further investigate whether electrical stimulation could enhance functional recovery, we recorded LFP activity in freely moving mice when punctate mechanical force was applied to the plantar hind paw using von Frey filaments. Mice that were transplanted with organoids and Naïve mice, were implanted with flexible electrodes into the S1 for LFP recordings during mechanical force application to assess the long-term neurological function. Our findings revealed that the energy in the Gamma and high-Gamma bands during the von Frey test in the BO-ET-ES group continued to increase over time, significantly surpassing that in the BO-ET group. Furthermore, the energy in the Gamma and high-Gamma bands of the BO-ET-ES group at 180 dpt was

Fig. 2 | Organoid brain-computer interface was constructed in vivo. **A** Schematic illustration of the organoid-brain-computer interfaces (OBCIs) in vivo. The red squares represent the stimulated sites. M1, primary motor cortex; S1, primary sensory cortex; Fig. 2A (the third figure) was created with BioRender.com; (**B**) Brightfield micrographs of grafts and mice brains with or without electrode insertion; (**C**) Overview of the OBCIs at 60 dpt. The white dotted line marks the electrode trace. The grafted organoid is shown in green. Scale bar: 500 μm. (a-d) represents the position relative to the electrode, which displayed protein expression in different regions. (C-a) Immunostaining for microglia (red) and graft (green) are shown at 60 dpt. The red dotted line marks the electrode traces. Scale bar: 50 μm. (C-b) Homeostatic microglia (P2RY12). Scale bar: 10 μm. (C-c) The activated microglia are marked with iNOS (red). Scale bar: 50 μm. (C-d) Markers for astrocyte (GFAP) at 60 dpt. Scale bar: 50 μm; (**D**) Overview of the electrode insertions in mouse brain at 60 dpt. Scale bar: 500 μm. Markers for microglia (D-a), astrocytes (GFAP, D-b), endothelial cells (CD31, D-c), and MAP2/SYN (D-d) at 60 dpt in mice brains are shown. Scale bar: 100 μm in D-a, b, 50 μm in D-c, 30 μm (left) and 10 μm (right) in D-d; (**E**) Markers for human nuclei (HN, red) and CD31 (green) at 120 dpt. Scale bar: 50 μm; (**F**–**H**) Immunostaining for MAP2 (**F**), DCX (**G**), and synapse (**H**) at 120 dpt in the grafts. Scale bar: 50 μm in F, 100 μm in G, 20 μm in H; (**I**) High-pass trace of electrophysiology in organoid in vivo at 30, 60, and 90 dpt. The red arrow indicates the identified spike; (**J**) Spectrograms derived from the entire electrodes in vivo at 30, 60, and 90 dpt; (**K**) The survival rate of grafted mice in the BO, BO-ET, and BO-ET-ES groups was calculated; (**L**) SNR analysis for the flexible electrodes at 60, 120, and 180 dpt, n = 9 (60, 120 180 dpt) mice, $^{**}P < 0.01$. Mean ± SD is shown for each condition. Statistical significance was tested by One-way ANOVA with Tukey's multiple comparison.

comparable to that of the Naïve group, suggesting functional recovery of the host in the BO-ET-ES group (Fig. 4P, Q). In addition to mechanically stimulating the von Frey, we applied thermal stimulation using the hot-plate test to evaluate the host's functional recovery. Our results demonstrated that the energy in the high-frequency band during the withdrawal of the hind paw was significantly higher in the BO-ET-ES group compared to the BO-ET group, and was similar to that of the Naïve group, which confirmed that stimulation promoted functional recovery in the host (Supplementary Fig. 7K-M). Furthermore, we assessed the cognitive and motor abilities of the mice to determine whether organoid grafts or stimulating in vivo would impact other neural functions. Our results indicated that there were no significant differences in new object recognition ability and motor abilities among the Naïve, BO, and BO-ET-ES groups at 75 dpt, suggesting that there were no discernible deficits in memory or locomotion in the mice (Supplementary Fig. 7N–Q).

Late-stage stimulation improved structural integration via the organoid-brain-computer interface

Considering that transplanted organoids extensively projected into the host brain at 60 dpt, we assessed their anatomical connections following late-stage stimulation to determine whether stimulation based on OBCIs can enhance structural integration within the grafts and the host. We established appropriate parameters by calculating the cross-correlation between the organoids and the host before and after stimulation, demonstrating that 70 Hz stimulation resulted in significantly higher connectivity between the grafts and the host compared to other parameters (Supplementary Fig. 8A, B). Similarly, the changes in firing rate and Gamma band energy induced by 70 Hz stimulation were significantly higher, consistent with the trend observed in cross-correlation (Supplementary Fig. 8C–I). Thus, 70 Hz stimulation was selected to modulate the grafts at the late stage (Fig. 5A, B). We observed representative images of robust graft survival in the BO, BO-ET, and BO-ET-ES groups at 120 dpt (Fig. 5C).

The functional integration of organoids with the host brain depends upon the establishment of connections between graft neurons and host brain circuits. We investigated the extent of graft projections into the host brain and their anatomical targets at 60, 120, and 150 dpt. The boundary of the organoids was hazy due to extensive projections into the host brain, with bundle-like projections also observed (Fig. 5D-c). Most projections were located adjacent to the graft (Fig. 5D-b, Supplementary Fig. 9A-b), while some were found in the contralateral cortex (Fig. 5D-a). Additionally, a greater number of projections were identified in both the ipsilateral and contralateral corpus callosum (CC) at various stages (Fig. 5D-d, f, Supplementary Fig. 9A-a, B-b, C-a). We also detected graft efferents in the hippocampal region at 120 and 150 dpt (Fig. 5D-g, Supplementary Fig. 9C-b). Furthermore, projections were observed in subcortical structures at 120 and 150 dpt, such as the ventral posterolateral nucleus (VPL), which were closely associated with the S1; none were observed at 60 dpt (Fig. 5D-i-j, Supplementary Fig. 9B-g, 9C-c, d). Projections extending over longer distances were noted at 150 dpt (Supplementary Fig. 9B-a, c-f, h). Comparative analysis indicated that late-stage stimulation enhanced the number of projections from organoids to the ipsilateral host brain, as evidenced by increased projection counts and longer distances (Fig. 5E, Supplementary Fig. 9D). The presence of $VGLUT1^+$ and glutamic acid decarboxylase 65 and 67 (GAD65/67) puncta suggested the existence of glutamatergic and GABAergic synapses (Fig. 5F, H). Our findings demonstrated that stimulation facilitated the establishment of excitatory and inhibitory synaptic connections between organoids and the host (Fig. 5G, I). Moreover, an increase in synaptic spine density in neurons was observed in the BO-ET-ES groups compared to the BO and BO-ET groups (Fig. 5J, K). Immunostaining for synapses showed multiple colocalized puncta of hSYN and PSD95, indicating synaptic connectivity within the grafts. Notably, synaptic connections from the organoids projecting into the host were examined at 60, 120, and 150 dpt (Fig. 5L, Supplementary Fig. 9E), demonstrating that late-stage stimulation significantly promoted the formation of functional synapses between organoids and the host (Fig. 5M, Supplementary Fig. 9F).

Late-stage stimulation ameliorated neurological function via the organoid-brain-computer interface

In addition to examining the structural integration between grafts and the host, we investigated the presence of electrophysiological function, particularly the signal connectivity between organoids and the host brain (Fig. 6A). Over a 10-day stimulation period, organoids exhibited consistent increases in spiking activity, as measured by firing rate, burst frequency, and burst duration. This indicated synaptic maturation of electrical transmission within the graft, suggesting that stimulation contributed to the functional development of the grafts (Fig. 6B–D). Notably, this trend was not observed in spike amplitude, indicating that the cellular action potentials of individual neurons remained stable (Fig. 6E). LFP measurements in the grafts revealed simultaneous oscillations in multiple frequencies, ranging from Delta to high-Gamma, which is characteristic of mature neural networks in vivo. A more pronounced and sustained increase in mid-high frequencies (Beta to high-Gamma) was observed in the BO-ET-ES group compared to the BO-ET group, suggesting that the stimulus activated oscillations within these frequency bands (Fig. 6F, G).

We further evaluated the connectivity and coupling of LFP. Firstly, the correlation within organoids (auto-correlation) and connections between organoids and hosts (cross-correlation) were analyzed. The results indicated that both types of correlations increased significantly 3 months after stimulation, with a more pronounced effect observed in the BO-ET-ES group (Fig. 6H–J). In the grafts, we noted a greater PAC between broadband low-frequency and Gamma activity following a 10-day stimulation, compared to the BO-ET group. This phenomenon was accompanied by a sustained increase in low-frequency-Gamma PAC in the grafts for 3 months post-stimulation, suggesting that electrical stimulation had a long-term impact on the dynamic development of neural networks (Fig. 6K). The LFP results demonstrated the

https://doi.org/10.1038/s41467-024-53858-2

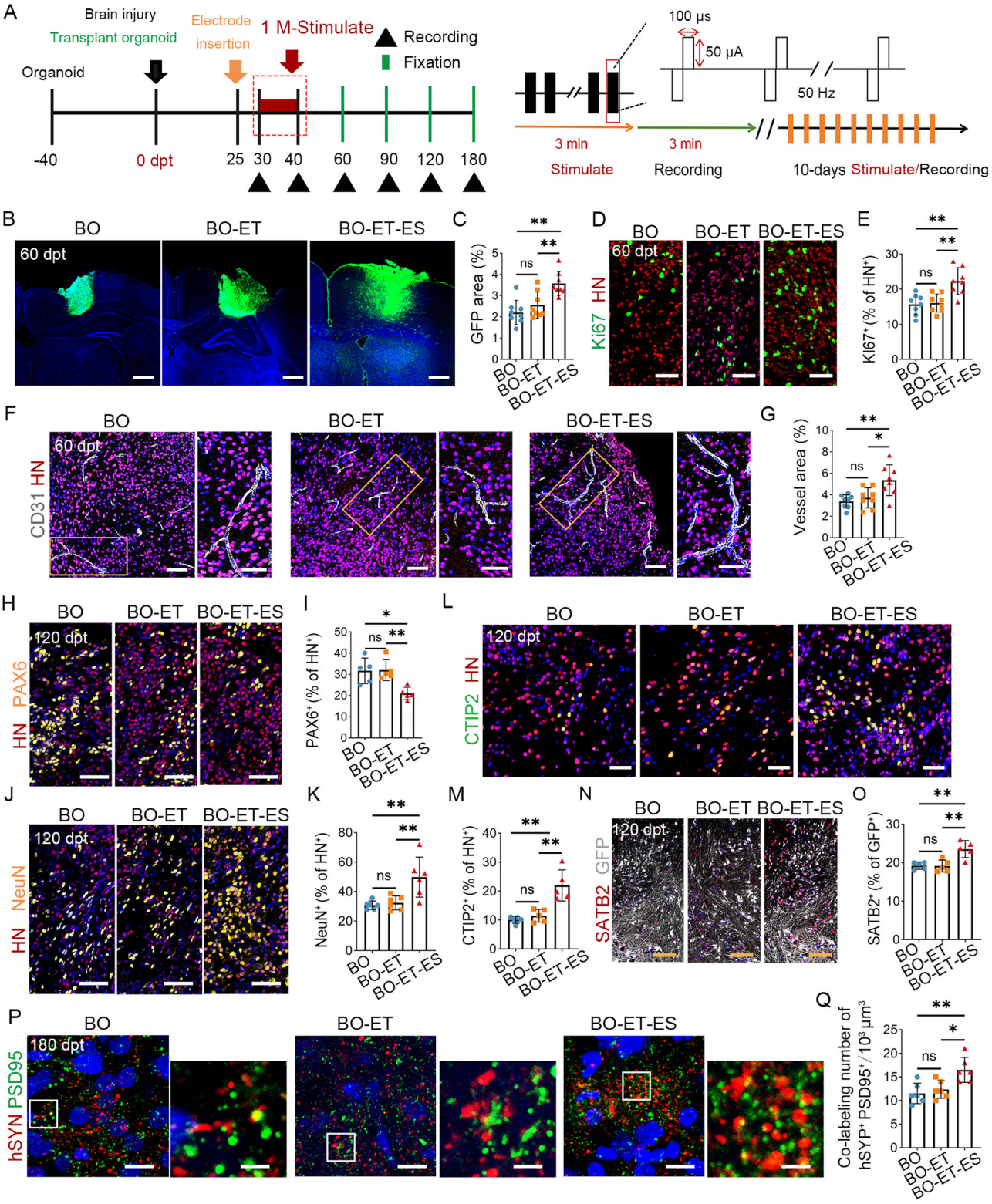

evolution of organoids across different network states and highlighted the correlation within the complex neural network formed by organoids and the host. Our analysis showed that both the correlation showed improvement during the 3 months following stimulation, with this enhancement being more significant in the BO-ET-ES group. These findings underscore the enduring effects of electrical stimulation on the connectivity of neural networks.

Similarly, we applied punctate mechanical force to the plantar hind paw using von Frey filaments as a behavior test. During mechanical stimulation, the activity across all frequency bands of the grafts was enhanced. This enhancement was most pronounced in the Gamma band, which is closely associated with pain, indicating that the grafts had integrated into functional circuits within the S1 cortex. During stimulation, the energy enhancement associated with mechanical pain in the mid-high frequency band and PAC of Theta-Gamma continued to increase, with more significant effects observed in the BO-ET-ES group (Supplementary Fig. 10A–F). Our results suggested that electrical stimulation consistently influenced the

Fig. 3 | Early-stage stimulation promoted the differentiation of organoid grafts via OBCIs. A This schematic illustrates the timeline for organoid implantation (0 dpt), electrode insertion, 1 M stimulation, and recording signals. The right figure shows detailed parameters of electrical stimulation; (**B**) Coronal sections of mice brains demonstrate organoid growth in the BO, BO-ET, and BO-ET-ES group at 60 dpt. BO, organoid implantation; BO-ET, organoid and electrode implantation without regulation; BO-ET-ES, BO-ET with electrical stimulation. Scale bar: 500 μm; (**C**) The organoid volumes are quantified in different groups, n = 6 grafts, $^{**}P < 0.01$; (**D**) The immunofluorescence staining for Ki67 (green) and human nuclei (HN, red) in three groups at 60 dpt. Scale bar: 50 μm; (**E**) Quantification of Ki67$^+$ cells show an increase in BO-ET-ES, n = 6 grafts, $^{**}P < 0.01$; (**F**) Immunofluorescence for HN and CD31 in different groups at 60 dpt. Scale bar: 100 μm (left) and 30 μm (right); (**G**) The vascular structures (CD31) are quantified, n = 6 grafts, $^{**}P < 0.01$; (**H**, **J**) Neural progenitors and mature neurons are identified with PAX6 (**H**) and NeuN (**J**) at 120 dpt. Scale bar: 50 μm in H, and 100 μm in J. (**I**, **K**) The expression of PAX6$^+$ and NeuN$^+$ cells are quantified, n = 3 grafts, $^{*}P < 0.05$, $^{**}P < 0.01$; (**L**) Immunofluorescence staining for CTIP2 (**L**) and SATB2 (**N**) at 120 dpt. Scale bar: 50 μm in **L**, and 100 μm in **N**; (**M**, **O**) Quantification of the CTIP2$^+$HN$^+$ cells and SATB2$^+$/GFP$^+$ cells are shown, n = 3 grafts, $^{**}P < 0.01$; (**P**) hSYN (red) and PSD95 (green) is displayed in the three groups at 180 dpt. Scale bar: 10 μm (left), and 3 μm (right); (**Q**) Quantification of the number of hSYN/PSD95 colocalized puncta at 180 dpt in the three groups, n = 3 grafts, $^{*}P < 0.05$, $^{**}P < 0.01$. Data are shown as mean ± SD, n = 8 images/6 mice in (**C**, **E**, **G**), n = 5 images/3 mice in (**I**, **M**, **O**, **Q**). n = 6 images/3 mice in (**K**). Statistical significance was tested by One-way ANOVA with Tukey's multiple comparison for **C**, **E**, **G**, **I**, **K**, **M**, **O**, **Q**.

integration of brain organoids into behavioral and functional neural circuits. Over the long term, the behavioral neural function of the grafts was monitored at 120 and 150 dpt. We found that the energy of the high-frequency band and Theta-Gamma coupling during von Frey application in the BO-ET-ES group were significantly higher than that in the BO-ET group, approaching levels observed in the Naïve group. This suggested that electrical stimulation promoted the recovery of behavioral function at a late stage (Fig. 6L–N).

Discussion

The significant burden of brain injury is largely attributed to its limited capacity for repair, which is constrained by restricted neurogenesis and axon regeneration. Studies have presented that generalized BCIs have the potential to sense and modulate brain neural activities, intending to restore function and enhance therapeutic outcomes. However, it is limited for neural interfaces to work well when a large cavity is caused. In light of the feasibility of using brain organoids as grafts, creative OBCI systems were constructed. We assessed the safety and viability of the OBCIs and investigated modulation strategies to regulate organoid development and their integration with the host brain. At various time points following grafting, we observed progressive maturation of the grafts and an increase in structural-functional connections between the grafts and the host brain after stimulation. This indicates that stimulation through OBCIs promotes functional recovery in the host.

DBS has been utilized to treat movement disorders, including Parkinson's disease[33], dystonia, and essential tremor[34], by delivering therapeutic stimulation to targeted areas via implanted BCIs[35]. Applying high-frequency DBS to the subthalamic nucleus can enhance downstream neural activity, thereby managing Parkinson's disease. This modulation affects both afferent and efferent brain regions, ultimately aiming to restore neural function[36]. Additionally, implantable BCIs have been reported to facilitate brain injury by promoting the survival and differentiation of endogenous NSCs[6,25], and modulating the plasticity of the brain tissue[7–9]. Notably, an electrical-cellular hybrid device, which combined implantable BCIs with exogenous NSCs, has been proven to enhance connection within transplanted cells and existing neural circuitry through regeneration and stimulation[27–29]. However, these devices face limitations when a large cavity is caused. 3D brain organoids, an ideal graft alternative, may address these problems[18–20]. Thus, it is both necessary and feasible to construct an OBCI system that integrates implantable BCIs with organoids. Our findings indicated that modulation via OBCIs promoted graft development and established functional connections with the host. Furthermore, bidirectional implantable BCIs have been demonstrated to decode brain activity and modulate brain network[33,37,38], suggesting that bidirectional OBCIs, which implement feedback and closed-loop regulation, are poised to provide a unique platform for disease modulation.

Building OBCIs presents several challenges, including difficulties with electrode insertion and the prolonged monitoring of functional signals. The implantation of flexible electrodes carries risks such as infection and bleeding, particularly due to the use of tungsten wire, which can compromise implantation accuracy and potentially cause irreversible damage[39]. In our study, the dural membrane was removed to alleviate the bleeding, and the implantation speed was controlled to minimize neural damage. For long-term monitoring, the major risks include reference instability and power frequency noise. To maintain the quality of our signal, the screws were periodically retightened, and Faraday shielding was applied around the mice. Additionally, we investigated the timing of electrode implantation. We attempted to insert electrodes simultaneously with transplantation of organoids to avoid a secondary craniotomy. However, this approach faced challenges due to the low elastic modulus and small size of the grafts. A study has reported that organoids decreased in size during the first 0–14 days after transplantation, which is the period before host vasculature infiltrates the graft[18]. This suggests that the first 14 days are critical for the survival of organoids, potentially affecting the growth of transplanted organoids when electrodes are implanted. Our previous study found that organoids exhibited superior growth after 25 days of implantation, which allowed for the coverage of the damaged cavity. Therefore, a time point beyond 25 days post-organoid transplantation can be selected as a suitable moment for electrode insertion. In addition, flexible microelectrodes with appropriate mechanical properties and excellent stability were utilized to record long term signals. OBCIs with better biocompatibility and effectiveness without glial cell aggregation around the electrode, are similar with existing studies[31,32]. Most microglia were not activated (R2RY12$^+$ and iNOS$^-$) and maintained a ramified morphology, and the grafts displayed good development for a long time. Furthermore, increasing complex functional signals of OBCIs were detected, indicating the functional maturity of the grafts and the prolonged effectiveness of electrodes.

Modulating strategies plays a crucial role in generalized BCIs while exploring suitable parameters for OBCIs, which have yet to be thoroughly investigated. Studies have reported that one of the most prevalent micro-stimulation signals is characterized by a constant-current, cathode-leading, biphasic square waveform, which has been suggested to be both safe and effective, reducing tissue damage by alternating the polarity of the pulse phases[40–42]. Notably, electrical stimulation was delivered at specific frequencies, voltages, and intervals, encoded with different input information to the brain organoids in the study conducted by Guo et al., utilizing planar microelectrode arrays (MEAs) in vitro to determine effective parameter[43]. Here, we innovatively constructed an organoid-electrode complex to simulate the OBCI system and investigate parameters that can activate brain organoids based on the platform. Unlike previous studies, we selected the mode of pulse current due to the instability of pulse current during voltage stimulation, which demonstrated effective parameters in the gradient exploration of amplitude ranging from 10 to 70 μA and frequency ranging from 1 Hz to 100 Hz. The mean firing rate of the response increased with the stimulus parameters, while no further increases

https://doi.org/10.1038/s41467-024-53858-2

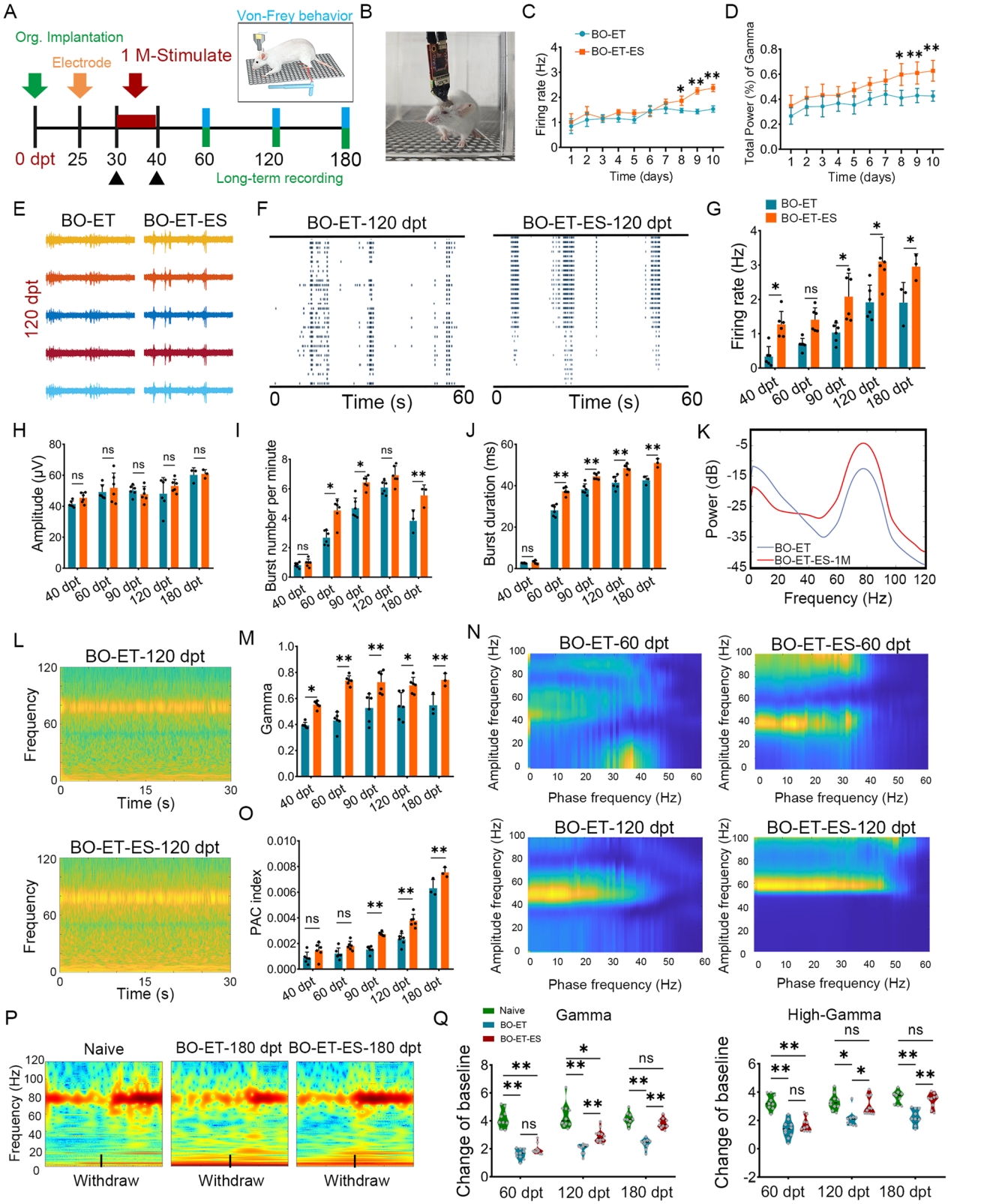

were observed beyond 50 Hz and 50 μA, respectively. Therefore, we selected 50 Hz and 50 μA as the stimulation parameters.

Brain stimulation has been shown to alleviate neurological disorders through mechanisms that include increased cell proliferation and migration in the SVZ[44–46], enhanced angiogenesis, and improved dendritic length and spine density[47,48]. Furthermore, implantable electrical-cellular hybrid devices can promote functional cellular integration with brain tissue and enhance synaptic connections[27,28]. The stimulation of NSC transplants has been found to improve brain recovery following a stroke, demonstrating superior outcomes compared to electrical regulation or NSC transplant therapy alone[29]. In this study, we investigated the neurodevelopment of grafts and their integration with the host brain using the OBCI system. Given that the 30-dpt organoids exhibited robust growth and maintained a high

Fig. 4 | Early-stage stimulation promoted functional maturation of organoids via OBCIs. A This schematic illustrates the timeline for early-stage stimulation; (**B**) Images of behavioral tests; (**C**, **D**) Electrophysiology of stimulated organoids in vivo at intervals of the day; (**C**) firing rate and (**D**) energy of Gamma band for LFP, n = 6 mice, $^{*}P < 0.05$ and $^{**}P < 0.01$; (**E**) High-pass trace of a representative 3-second recording at 120 dpt; (**F**) Raster plot for 60 seconds at 120 dpt; (**G**–**J**) Electrophysiology of organoids in vivo after stimulation at 40, 60, 90, 120, and 180 dpt. (**G**) firing rate, (**H**) spike amplitude, (**I**) burst number per min, and (**J**) burst duration, n = 6 mice (40, 60, 90 and 120 dpt) and n = 3 mice (180 dpt), $^{*}P < 0.05$ and $^{**}P < 0.01$; (**K**–**L**) Power spectral density and spectrogram from the entire recordings at 120 dpt. (**K**) Power spectral density and (**L**) Spectrogram; (**M**) Quantifying total power percentage of Gamma in vivo at 40, 60, 90, 120, and 180 dpt, n = 6 mice (40, 60, 90 and 120 dpt) and 3 (180 dpt), $^{*}P < 0.05$ and $^{**}P < 0.01$; (**N**) Intensity distribution of PAC at 60 and 120 dpt; (**O**) Theta-Gamma PAC quantifications of organoids in vivo after stimulation at 40, 60, 90, 120, and 180 dpt, n = 6 mice (40, 60, 90 and 120 dpt) and n = 3 mice (180 dpt), $^{**}P < 0.01$; (**P**) Spectrograms derived from the entire electrodes in the Naïve, BO-ET-ES and BO-ET groups during withdrawal in the von Frey test at 180 dpt; (**Q**) Change of total power percentage of Gamma and high Gamma and Theta-Gamma coupling post withdrawal compared to baseline in the Naïve, BO-ET-ES and BO-ET groups in the von Frey test at 60, 120, and 180 dpt, n = 9 withdraws (60 dpt in Naïve), 10 withdraws (120 dpt in Naïve), 9 withdraws (180 dpt in Naïve), 10 withdraws (60 dpt in BO-ET), 9 withdraws (120 dpt in BO-ET), 9 withdraws (180 dpt in BO-ET), 10 withdraws (60 dpt in BO-ET-ES), 12 withdraws (120 dpt in BO-ET-ES) and 9 withdraws (180 dpt in BO-ET-ES) from 3 mice in each group, $^{*}P < 0.05$ and $^{**}P < 0.01$. Data is shown as Mean ± SD. Statistical significance was tested with Two-way ANOVA for **C**, **G**–**J**, **O**, and **Q**.

proliferative capacity, we regulated graft development during the stage. At the later stage (60 dpt), the grafts are extensively projected into the host brain. Consequently, we mainly explored the integration between the grafts and the host brain. The parameters of 50 Hz and 50 μA were verified in vitro and performed for 20 days in vivo via OBCIs, displaying a decreased firing rate after 10 days due to overactivation of the neurons. This finding indicated that a 10-day modulation period was appropriate for the OBCIs. Our results demonstrated an increase in graft volume, a higher number of proliferative cells (as indicated by Ki67 and PAX6), and enhanced vascular infiltration (CD31) following early-stage stimulation. Notably, our findings also indicated that electrical modulation promoted the progressive differentiation of neurons within the grafts, consistent with previous 2D studies[25,49].

Studies have documented that stimulation in the somatosensory cortex creates a frequency-dependent activation density pattern[50]. Increasing frequency may lead to transient activation of axons localized to the electrode. High-frequency stimulation of axons, such as at 100–200 Hz, has been proven to disrupt the synchronicity of evoked responses compared to 50 Hz[51]. Here, we explored appropriate frequencies ranging from 1 Hz to 100 Hz to modulate grafts via OBCIs at 60 dpt. Our findings indicated that stimulation at 70 Hz exhibited the highest graft-host correlation. It has been reported that the sign and magnitude of synaptic potentiation are heavily dependent on the frequency and pattern of stimulation, which can alter connectivity within a cortical area[52,53]. Our findings indicated that stimulation promoted an increase in projections from organoid grafts, targeting sensory-related regions such as the cortex, thalamus, hippocampus, and VPL, associated with pain perception. Moreover, we found that stimulation at 60 dpt influenced synapse formation, including both excitatory (VGLUT1) and inhibitory (GAD65) synapses. The functional maturity of organoids was also enhanced by electrical stimulation, as evidenced by shorter ISI, higher firing rates, and an increased number of burst events. Gamma oscillations have been implicated in cognitive functions, the regulation of synaptic plasticity, and long-range communication between brain regions. Pain-related oscillatory activity at high Gamma frequencies (>40 Hz) in S1 was reported to correlate with the intensity of stimulation and subjective pain[54]. Our research found that Gamma band energy was significantly higher after electrical stimulation.

Higher throughput, ultra-flexible, and multifunctional electrodes —capable of electrical or light stimulation and drug delivery—are expected to become mainstream in electrode technologies of the future, aiming to achieve high spatial resolution, long-term stability, and multifunctional monitoring[55]. Additionally, progress in implantation technology, including precise electronic devices and the integration of compliant electrodes with auxiliary tools[56], is anticipated to enhance the accuracy of electrode implantation while reducing the risk of nerve injury. Although we have developed OBCI systems and implemented OBCI-based regulation, several limitations remain that cannot be overlooked. Concerns regarding organoid and electrode implantation include the prolonged survival of both the host and graft, as well as the potential tumorigenicity of the graft, which must be monitored over extended periods[18,57]. Our findings indicated no significant difference in the survival rates of mice across different groups, and the grafts exhibited robust growth following regulation. Additionally, our results showed that no tumors formed in the grafts, which were OCT4/SSEA4 negative and demonstrated progressive maturity, indicating their safety. In the future, the uncertainties introduced by the implantation process and the unknown distribution of the host neural network necessitate clarification regarding the biological interpretations based on the data recorded by each electrode. In addition, our study integrated organoids with bioelectronics in vivo, creating a system that facilitates more intuitive communication with the brain, which holds promise for applications in brain injury, prosthetics, and bidirectional brain-machine interfaces.

Methods

Characterization and maintenance of H9- hESCs cells

Human embryonic stem cell lines (hESCs) (WiCell Agreement No. 24-W0484) were used in this study. GFP-H9 colonies were expanded on 6-well tissue cultured plates with Matrigel-coated (Corning, USA). hESCs were cultured with mTeSR plus medium (StemCell Technologies, Vancouver, Canada) and passaged every 4–5 days at a ratio of 1:30 using 0.5 mM EDTA solution (Nuwacell). Cells were cultured in a humidified 37 °C incubator with 5% CO_2 and were fed daily. Cultures maintained negative for mycoplasma with the MycoAlert Kit (Lonza).

Animals care

All animal experiments were approved by the Animal Care and Use Committee of Tianjin University (TIVE-2021-128). Immune-deficient non-obese diabetic (NOD)/ severe combined immunodeficient (SCID) mice (male), aged 4-6 weeks, were purchased from Beijing Vital River Laboratory Animal Technology Co., Ltd (Beijing, China). The NOD-SCID mice were kept in autoclaved cages with up to 5 mice per cage under standard conditions (25 °C ± 1 °C, 40%-70% relative humidity) on a 12 h light/dark cycle with free access to food and water. The feed and bedding of mice were all replaced in the super clean bench.

In this study, mice were randomly assigned into BO (transplant brain organoids only in the host brain), BO-ET (organoid brain-computer interface in vivo without electrical stimulation), and BO-ET-ES (organoid brain-computer interface in vivo with electrical stimulation) groups. Before electrode implantation, one mouse died. At early stage, electrode was inserted at 25 dpt, one mouse died at 40 dpt. The signal quality of two mice was deemed inadequate during the long-term recording process and they were subsequently excluded from further experiments. At the late stage, there was no mouse sacrificed after electrode implantation. One mouse was excluded due to signal quality. The number of mice in each group as following: BO: 25, BO-ET: 30, and BO-ET-ES: 30.

Generation of brain organoids

For generation of human brain organoids (hBOs), hESCs were dissociated with Accutase ((Life Technologies, USA) and 9000 cells / well

https://doi.org/10.1038/s41467-024-53858-2

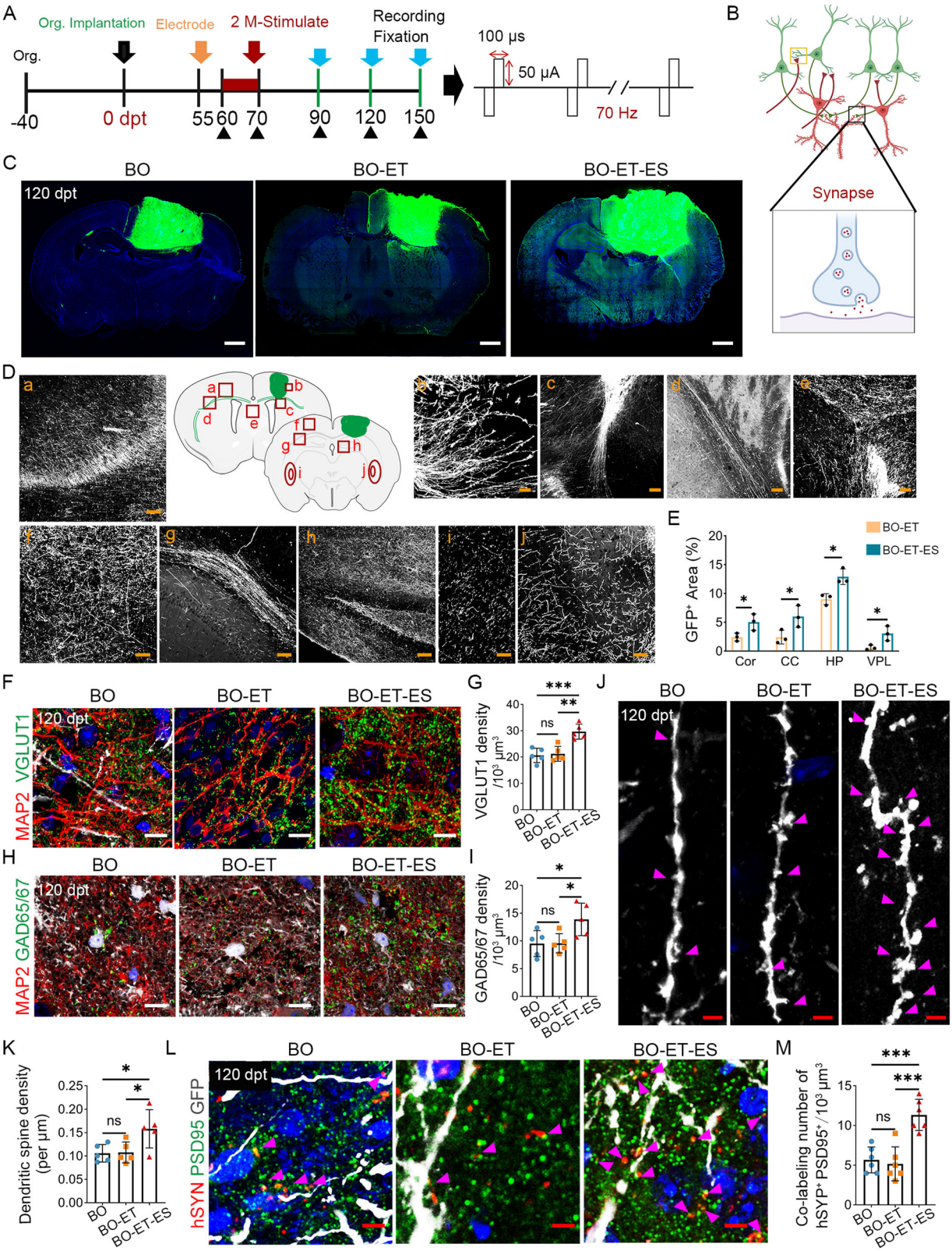

was plated into the ultralow-attachment 96-well plates (Corning Costar) in the neural induction medium (NIM) from D0-D10 (NIM medium: DF12, 15% [v/v] KOSR, 1% [v/v] GlutaMAX, 1% [v/v] NEAA [all Gibco, USA], 100 μM β-Mercaptoethanol [Sigma, Germany], 100 nM LDN193189 [Sigma, Germany], 10 μM SB431542 [Abcam, England], 2 μM XAV939 [Sigma, Germany], 50 μM Y27632 [Stem Cell Technologies, Canada]). The media was half-changed every other day with NIM without Y27632. On day 10, EBs were transferred into 6-well plate and cultured in differentiation medium (DIM) (50% DMEM/F12, 50% Neurobasal medium, 1% [v/v] N2 supplement, 1% [v/v] B27 supplement minus vitamin A, 0.5% [v/v] NEAA, 1% [v/v] GlutaMAX, 1% [v/v] Penicillin/Streptomycin [all Gibco, USA], 0.025% Insulin [Sigma, Germany], 50 μM β-Mercaptoethanol [Sigma, Germany]), and cultured on an orbital shaker (80 rpm at 37 °C) (IKA, KS260, Germany). After that, the

Fig. 5 | Late-stage stimulation promoted the structural integration between organoids and the host via OBCIs. A This schematic illustrates the timeline for late-stage stimulation (60 dpt, left), and detailed parameter (right); (**B**) This schematic establishes the graft-host or host-graft synaptic structure; (**C**) Coronal sections of mice brains are shown at 120 dpt in the different groups. Scale bar: 500 μm; (**D**)(a-j) High magnification views of the transplanted organoid on a coronal section show a high density of GFP^+ projections. (a) contralateral cortex; (b-c) ipsilateral cortex, adjacent graft; (d) ipsilateral corpus callosum; (e-f) contralateral cortex; (g) contralateral corpus callosum and hippocampus; (h) ipsilateral hippocampus; (i) contralateral ventral posterolateral thalamus nucleus (VPL); (j) ipsilateral VPL. Scale bar: 50 μm in (a), (c-e) and (g-h),10 μm in (b), 20 μm in (f, i, j); (**E**) The GFP^+ projections are quantified in ipsilateral brain regions at 120 dpt in BO-ET and BO-ET-ES, n = 3 grafts; (**F**, **H**) Staining for MAP2/ VGLUT1 and MAP2/GAD65/67 in grafts at 120 dpt. Scale bar: 20 μm; (**G**, **I**) VGLUT1 and GAD65/67 density is quantified at 120 dpt in three groups, n = 3 grafts, $^*P < 0.05$, $^{**}P < 0.01$, $^{***}P < 0.001$; (**J**) Dendritic branches from BO, BO-ET, and BO-ET-ES grafts at 120 dpt are shown. The red triangle marks the dendritic spines. Scale bar: 5 μm; (**K**) Dendritic spine density is quantified at 120 dpt, n = 3 grafts, $^*P < 0.05$; (**L**) Staining for hSYN (red), PSD95 (green), and GFP (white) at 120 dpt. The red arrow indicates the colocalization of hSYN and PSD95. Scale bar: 5 μm; (**M**) Quantification of the number of hSYN/PSD95 colocalized puncta at 120 dpt, n = 3 grafts, $^{***}P < 0.001$. Data are shown as mean ± SD, n = 5 images/3 mice in (**G**, **I**, **K**, **M**). Statistical significance was tested by One-way ANOVA with Tukey's multiple comparison for **G**, **I**, **K**, **M**. The schematic illustrates in Fig. 5B (BioRender.com/d87u058) and 5D (BioRender.com/t24s318) were created with BioRender.com.

organoids were maintained in mature media consisting of 50% DMEM-F12, 50% Neurobasal medium, 1% [v/v] N2 supplement, 1% [v/v] B27 supplement, 0.5% [v/v] NEAA, 1% [v/v] GlutaMAX, 0.025% Insulin, 50 μM β-Mercaptoethanol, 1% [v/v] Penicillin/ Streptomycin, 20 ng/ml BDNF (PeproTech, USA), 200 μM L-ascorbic acid (Sigma, Germany). Media changes were performed every 4 days.

Organoid transplantation

The transplantation of organoids was performed as mentioned before[18]. The surgical procedure was carried out on a super-clean bench to maintain sterility. Organoids that passed strict quality control (visible ventricular zone (VZ)-like regions and cortical plate expansion) were selected for transplantation. Mice were anesthetized with 3% (induction) and 1.5% (maintenance) isoflurane in oxygen and mounted on a stereotactic frame. The skin above the skull was cut, and a ~ 0.5 mm diameter craniotomy centered at AP: 0.46 mm posterior to bregma and ML: 1.2 mm was performed with a hand-held drill. After removing the dura mater, a cavity (0.5 mm diameter and 0.8 mm depth) was created using vacuum aspiration with a blunt-tip needle attached to a vacuum line. The aspirated lesion was made unilaterally. hBOs were cut into 1-mm-diameter pieces using micro-scissors, and one piece of organoids was transplanted into a cavity. The cranial window was closed by recovering the bone flap, and the skin was closed with a suture. The temperature of mice was supported using a heating pad (Rayward Life Technology Co., Ltd, China).

Flexible electrode implantation in vitro and in vivo

In vivo, a 2-shank 64-channel high-density flexible electrode (each site: 16 × 12 μm) (NSDS, NeuroXess) was implanted when organoids were transplanted for 1 month or 2 months (BO-ET-30 dpt or BO-ET-60 dpt). The center-to-center distance of the electrode site was 60 μm with a total length of 1.86 mm. Mice were anesthetized with 5% (induction) and 1–2% (maintenance) isoflurane in oxygen. The prior incision was exposed to confirm the surviving hBOs with UV light that could be distinguished from the host brain. Electrode implantation was performed with the aid of a stereomicroscope. The flexible electrode was inserted incrementally with the stereotaxis apparatus (Rayward Life Technology Co., Ltd, China). One shank was inserted into the organoid, and the other was targeted to the host brain 1000 μm away from grafts. To prevent mechanical strain-related neural damage by microelectrode insertion, the tissue was allowed to rest for 1 min per 100 μm after insertion. A reference and ground screws were implanted into the skull overlying the cerebellum, secured with dental adhesive.

Electrophysiology recordings and stimulating strategy

For recordings of organoids in vitro, the implanted flexible electrodes were used to detect spontaneous neural activity of organoids from D90 to D120. The firing of neurons was recorded and modulated using an RHS Stim/Recording System (Intan), which had a sample rate of 30 kHz. For the stimulation of brain organoids in vitro, we conducted a comprehensive analysis of the amplitude and frequency parameters associated with current stimulation. By applying bipolar pulses with different parameters (current amplitude: 10 ~ 70 μA, frequency: 1, 10, 30, 50, 70, and 100 Hz), the responding neural activity was recorded and analyzed. Subsequently, we identified the optimal parameters for neuronal activation (50 μA at a frequency of 50 Hz).

For recordings of brain organoids in vivo, the flexible shank in the graft was used to detect the neural activity of organoids, and the other shank was inserted to detect the neural activity of the host. The firing of neurons was recorded and modulated using an RHS Stim/Recording System (Intan), which had a sample rate of 30 kHz. We employed the suitable stimulated parameter according to the existing studies with minor modifications 37,38. In vivo, we further explored the appropriate duration for stimulation based on their response. For stimulation at 60 dpt, we determined stimulated frequency referring to the cross-correlation between graft-host response. We successfully stimulated the grafts at 10, 30, 50, 70, and 100 Hz, resting for 10 min after each stimulation to avoid interference with the following stimulation. The cross-correlation between the organoids and the host was analyzed. In the BO-ET-30 dpt group, 6 mice were used for 60-dpt experiments, 6 mice for 120-dpt experiments, and 3 mice to explore suitable stimulated parameters. In the BO-ET-60 dpt group, 6 mice were used for 90-dpt experiments, 6 mice were used for 120-dpt, and 3 mice were utilized to explore appropriate frequency. Long-term signal recordings and behavior tests were also performed in the BO-ET-60 dpt group at 120 dpt.

Immunofluorescence and image analysis

For immunostaining of organoids and brain slices, cryosections were washed with PBS, permeabilized in 0.3% Triton X-100 in PBS for 15 min, and 10% goat serum was used to block for 1 h at room temperature (RT). After that, slides were incubated in the primary antibody diluted in 10% goat serum at 4 °C overnight. The next day, the sections were washed 3 times (5 min each time) with PBS and then incubated with secondary antibodies for 1 h at RT. Finally, it was counter-stained with DAPI for 15 min after washing 3 times and mounted with ProLong Gold Antifade Reagent (ThermoFisher). All image data were captured and processed using a confocal microscope system (Nikon A1HD25). Area-scale image series were analyzed, and the numbers of positive cells for each marker and the length of the ventricular zone (VZ) and (cortical plate) CP layers were measured using Fiji software; at least 5 random regions were chosen.

Behavioral tests

All behavioral tests were carried out during the light cycle of the animals. Mice underwent 30-min acclimatization in the box used for the pain behavior test. Mechanical sensitivities of the hind paw in the contralateral side of the implanted brain organoid were assessed using the graded von Frey filaments forces (Touch-Test™, NC12775) to the plantar surface of the paw. Each mouse was tested with different forces ranging from 0.04 g to 2 g, and each parameter was performed five times. The experiment stopped when the mouse showed 5 withdrawal

https://doi.org/10.1038/s41467-024-53858-2

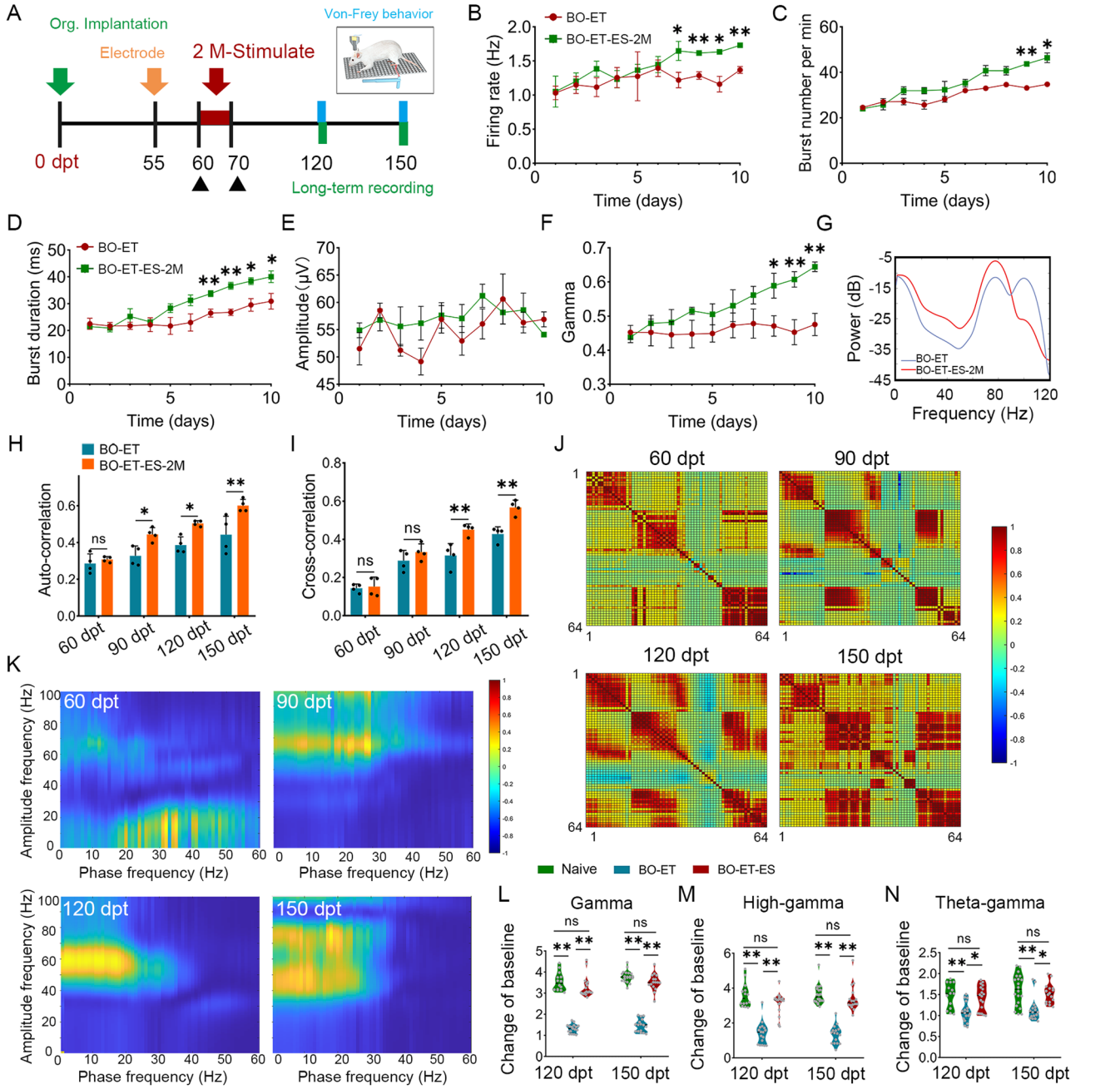

Fig. 6 | Late-stage stimulation promoted the functional integration between organoids and the host via OBCIs. A This schematic illustrates the timeline for 2 M stimulation; (**B**–**E**) Spiking quantifications of stimulated organoids in vivo at intervals of the day. (**B**) firing rate, (**C**) burst number, (**D**) burst duration, and (**E**) spike amplitude, n = 4 mice, $^{*}P < 0.05$ and $^{**}P < 0.01$; (**F**) Energy of frequency band at Gamma of stimulated organoids in vivo at intervals of the day, n = 4 mice, $^{*}P < 0.05$ and $^{**}P < 0.01$; (**G**) Power spectral density at 150 dpt; (**H**–**I**) Correlation coefficient quantifications of organoids in vivo after stimulation at approximately monthly intervals initiating at day 60. (**H**) auto-correlation inside organoids, and (**I**) cross-correlation between organoids and host, n = 4 mice, $^{*}P < 0.05$ and $^{**}P < 0.01$; (**J**) Coefficient distribution of correlation at 60, 90, 120, and 150 dpt in the BO-ET-ES group; (**K**) The BO-ET-ES group has an intense distribution of PAC at 60, 90, 120, and 150 dpt; (**L**–**N**) Change of total power percentage of Gamma and high Gamma, and Theta-amma coupling post withdrawal compared to baseline in the Naïve, BO-ET-ES and BO-ET groups in vivo at 120, and 150 dpt, n = 14 withdraws (Naïve), 17 withdraws (BO-ET) and 18 withdraws (BO-ET-ES) from 4 mice (120 dpt) and n = 20 withdraws (Naïve), 16 withdraws (BO-ET) and 18 withdraws (BO-ET-ES) from 3 mice (150 dpt), $^{*}P < 0.05$ and $^{**}P < 0.01$. Mean ± SD is shown for each condition. Statistical significance was tested with Two-way ANOVA for multiple comparisons in **B**–**F**, **I**, and **K**.

responses to a force. We used a high-speed camera (60 fps) to record the behavior track of mice, with a MATLAB program to synchronize the electrophysiological recording with the behavioral video recording.

Novel object recognition test

According to previous study, two different objects (orange cylinder and green cuboid) were used in this test, which had similar heights and volumes but differed in their appearance[14]. Firstly, mice were placed into a black square plastic area (40 cm × 40 cm × 40 cm) and explored the arena for 5 min. On the next day, the mice initially underwent a training session during which they were placed in the arena and explored the arena for 5 min with two identical objects. For the test, the mice were reintroduced into the arena for 5 min and one of the objects was substituted with a different one. Interaction, defined as the

mice directing their nose towards an object within 2 cm of the object, was manually scored by an experimenter who had no knowledge of the experimental group. After each training and test, the items and the field were cleaned. Finally, the index for the test period is calculated as (time spent using the new object - time spent using the familiar object)/(time spent using the new object + time spent using the familiar object).

Hot-plate test

According to previous study, the pain response of NOD-SCID mice in the Naïve, BO-ET, and BO-ET-ES groups were evaluated by the hot plate test[58]. Briefly, the animals were placed on a hot plate meter at 55 °C, and the time from when the two hind legs touched the hot plate to when the hind legs exhibited reactions such as shaking, jumping, or licking was measured. Each animal was tested three times with an interval of 15 min, and the average of the three response times was regarded as the final pain threshold for the mice. The observer was blinded to the experimental treatment. At the same time, we recorded the electrical signals of the mice to perceive and respond to the pain perception, and further analyzed them.

Neural signals analysis

Raw data were converted to.mat files and analyzed offline via custom MATLAB (The Mathworks Inc.MA, USA). The 50 Hz power frequency interference was filtered out, and the channel with excessive noise amplitude was eliminated. The signal was divided into low-frequency parts (0–300 Hz) and high-frequency parts (300–3000 Hz), in which the low-frequency part was used to analyze the local field potential (LFP) characteristics, and the high-frequency part was screened for spike detection. Spikes with stereotypical waveforms distinguished from noise and relatively high SNR were tagged and saved for further analysis. LFP data was resampled at 1000 Hz, and power values and information entropy were calculated for different frequency bands: 3–8 Hz (Theta), 8–13 Hz (Alpha), 13–30 Hz (Beta), 30–60 Hz (low Gamma), and 60–100 Hz (high Gamma).

For LFP analysis, the energy of each frequency band was performed using the Fourier transform, and the wavelet transform was used to conduct a time-frequency analysis. The correlation of different channels was calculated using the Pearson correlation coefficient. For phase-amplitude coupling (PAC), the Laplace transform was used to obtain the instantaneous phase and amplitude of each frequency band. Considering the PAC degree, we calculated the MI value between any two frequency bands and finally formed an MI matrix through which we directly observed PAC across the spectrum. For spikes, we calculated the standard deviation (δ) of the high-frequency part of the data, then data points lower than −5*δ were considered spike points. The firing rate, average spike amplitude, and inter-spike interval (ISI) of each channel were quantified, and burst detection according to the maximum inter-spike interval and the minimum spike number in a burst was carried out.

Statistics and reproducibility

Graphs and statistical analyses were generated using Prism 9 (GraphPad) and MATLAB software. A One-way ANOVA was used to compare multiple groups. Unpaired Student's t-test (two-tailed) was used to compare the two groups. Two-way ANOVA was performed. The specific statistical tests performed for each analysis are indicated in the corresponding figure legend. All data represent the mean values ± SD. Differences were considered significant when the P value was <0.05. Data shown from representative experiments were repeated with similar results in at least three independent biological replicates, unless otherwise noted. Behavioral experiments were performed blinded. We used the cubic curve fitting method to observe the trend for the data that could not be counted.

Reporting summary

Further information on research design is available in the Nature Portfolio Reporting Summary linked to this article.

Data availability

All data supporting the findings of this study are available within the article and its supplementary files. Any additional requests for information can be directed to, and will be fulfilled by, the corresponding authors. Source data are provided with this paper.

References

1. Hankey, G. J., Jamrozik, K., Broadhurst, R. J., Forbes, S. & Anderson, C. S. Long-term disability after first-ever stroke and related prognostic factors in the Perth Community Stroke Study, 1989–1990. *Stroke* **33**, 1034–1040 (2002).
2. Kempermann, G. et al. Human adult neurogenesis: evidence and remaining questions. *Cell Stem Cell* **23**, 25–30 (2018).
3. Wolpaw, J. R., Birbaumer, N., McFarland, D. J., Pfurtscheller, G. & Vaughan, T. M. Brain-computer interfaces for communication and control. *Clin. Neurophysiol.* **113**, 767–791 (2002).
4. Chaudhary, U., Birbaumer, N. & Ramos-Murguialday, A. Brain-computer interfaces for communication and rehabilitation. *Nat. Rev. Neurol.* **12**, 513–525 (2016).
5. Patel, S. R. & Lieber, C. M. Precision electronic medicine in the brain. *Nat. Biotechnol.* **37**, 1007–1012 (2019).
6. Willand, M. P., Nguyen, M. A., Borschel, G. H. & Gordon, T. Electrical stimulation to promote peripheral nerve regeneration. *Neurorehabil. Neural Repair* **30**, 490–496 (2016).
7. He, L. et al. Electrical stimulation at nanoscale topography boosts neural stem cell neurogenesis through the enhancement of autophagy signaling. *Biomaterials* **268**, 120585 (2021).
8. Brus-Ramer, M., Carmel, J. B., Chakrabarty, S. & Martin, J. H. Electrical stimulation of spared corticospinal axons augments connections with ipsilateral spinal motor circuits after injury. *J. Neurosci.* **27**, 13793–13801 (2007).
9. Wang, L. C., Wei, W. Y. & Ho, P. C. Short-term cortical electrical stimulation during the acute stage of traumatic brain injury improves functional recovery. *Biomedicines* **10**, 1965 (2022).
10. Aregueta-Robles, U. A., Woolley, A. J., Poole-Warren, L. A., Lovell, N. H. & Green, R. A. Organic electrode coatings for next-generation neural interfaces. *Front Neuroeng.* **7**, 15 (2014).
11. Wang, Y. et al. Modeling human telencephalic development and autism-associated SHANK3 deficiency using organoids generated from single neural rosettes. *Nat. Commun.* **13**, 5688 (2022).
12. Di Lullo, E. & Kriegstein, A. R. The use of brain organoids to investigate neural development and disease. *Nat. Rev. Neurosci.* **18**, 573–584 (2017).
13. Groveman, B. R. et al. Human cerebral organoids as a therapeutic drug screening model for Creutzfeldt-Jakob disease. *Sci. Rep.* **11**, 5165 (2021).
14. Revah, O. et al. Maturation and circuit integration of transplanted human cortical organoids. *Nature* **610**, 319–326 (2022).
15. Cao, S. Y. et al. Cerebral organoids transplantation repairs infarcted cortex and restores impaired function after stroke. *NPJ Regen. Med* **8**, 27 (2023).
16. Jgamadze, D. et al. Structural and functional integration of human forebrain organoids with the injured adult rat visual system. *Cell Stem Cell* **30**, 137–152.e137 (2023).
17. Wilson, M. N. et al. Multimodal monitoring of human cortical organoids implanted in mice reveal functional connection with visual cortex. *Nat. Commun.* **13**, 7945 (2022).
18. Mansour, A. A. et al. An in vivo model of functional and vascularized human brain organoids. *Nat. Biotechnol.* **36**, 432–441 (2018).

19. Kitahara, T. et al. Axonal extensions along corticospinal tracts from transplanted human cerebral organoids. *Stem Cell Rep.* **15**, 467–481 (2020).
20. Wang, Z. et al. Cerebral organoids transplantation improves neurological motor function in rat brain injury. *CNS Neurosci. Ther.* **26**, 682–697 (2020).
21. Meng, X. et al. Electric field-controlled directed migration of neural progenitor cells in 2D and 3D environments. *J. Vis. Exp.* 3453 (2012).
22. Feng, J. F. et al. Electrical guidance of human stem cells in the rat brain. *Stem Cell Rep.* **9**, 177–189 (2017).
23. Patil, N. et al. Electrical stimulation affects the differentiation of transplanted regionally specific human spinal neural progenitor cells (sNPCs) after chronic spinal cord injury. *Stem Cell Res. Ther.* **14**, 378 (2023).
24. Liu, Q. et al. Electric field stimulation boosts neuronal differentiation of neural stem cells for spinal cord injury treatment via PI3K/Akt/GSK-3β/β-catenin activation. *Cell Biosci.* **13**, 4 (2023).
25. Yang, H. et al. Gold nanostrip array-mediated wireless electrical stimulation for accelerating functional neuronal differentiation. *Adv. Sci. (Weinh.)* **9**, e2202376 (2022).
26. Stieglitz, T., Ruf, H. H., Gross, M., Schuettler, M. & Meyer, J. U. A biohybrid system to interface peripheral nerves after traumatic lesions: design of a high channel sieve electrode. *Biosens. Bioelectron.* **17**, 685–696 (2002).
27. Rochford, A. E., Carnicer-Lombarte, A., Curto, V. F., Malliaras, G. G. & Barone, D. G. When bio meets technology: biohybrid neural interfaces. *Adv. Mater.* **32**, e1903182 (2020).
28. Adewole, D. O., Serruya, M. D., Wolf, J. A. & Cullen, D. K. Bioactive neuroelectronic interfaces. *Front Neurosci.* **13**, 269 (2019).
29. Oh, B. et al. Electrical modulation of transplanted stem cells improves functional recovery in a rodent model of stroke. *Nat. Commun.* **13**, 1366 (2022).
30. Purushothaman, G., Scott, B. B. & Bradley, D. C. An acute method for multielectrode recording from the interior of sulci and other deep brain areas. *J. Neurosci. Methods* **153**, 86–94 (2006).
31. Luan, L. et al. Ultraflexible nanoelectronic probes form reliable, glial scar-free neural integration. *Sci. Adv.* **3**, e1601966 (2017).
32. Tian, Y. et al. An ultraflexible electrode array for large-scale chronic recording in the nonhuman primate brain. *Adv. Sci. (Weinh.)* **10**, e2302333 (2023).
33. Little, S. et al. Adaptive deep brain stimulation in advanced Parkinson disease. *Ann. Neurol.* **74**, 449–457 (2013).
34. Hariz, M. Twenty-five years of deep brain stimulation: celebrations and apprehensions. *Mov. Disord.* **27**, 930–933 (2012).
35. Mei, S. et al. Techniques of frameless robot-assisted deep brain stimulation and accuracy compared with the frame-based technique. *Brain Sci* **12**, 906 (2022).
36. Johnson, M. D., Vitek, J. L. & McIntyre, C. C. Pallidal stimulation that improves parkinsonian motor symptoms also modulates neuronal firing patterns in primary motor cortex in the MPTP-treated monkey. *Exp. Neurol.* **219**, 359–362 (2009).
37. Arlotti, M. et al. A new implantable closed-loop clinical neural interface: first application in Parkinson's disease. *Front Neurosci.* **15**, 763235 (2021).
38. Pulliam, C. L., Stanslaski, S. R. & Denison, T. J. Industrial perspectives on brain-computer interface technology. *Handb. Clin. Neurol.* **168**, 341–352 (2020).
39. Shen, K., Chen, O., Edmunds, J. L., Piech, D. K. & Maharbiz, M. M. Translational opportunities and challenges of invasive electrodes for neural interfaces. *Nat. Biomed. Eng.* **7**, 424–442 (2023).
40. Chen, Z. et al. An overview of in vitro biological neural networks for robot intelligence. *Cyborg. Bionic Syst.* **4**, 0001 (2023).
41. Tomaskovic-Crook, E. et al. Human neural tissues from neural stem cells using conductive biogel and printed polymer microelectrode arrays for 3D electrical stimulation. *Adv. Health. Mater.* **8**, e1900425 (2019).
42. Lilly, J. C., Hughes, J. R., Alvord, E. C. Jr & Galkin, T. W. Brief, noninjurious electric waveform for stimulation of the brain. *Science* **121**, 468–469 (1955).
43. Cai, H. W. et al. Brain organoid reservoir computing for artificial intelligence. *Nat. Electron.* **6**, 1032–1039 (2023).
44. Watson, M., Dancause, N. & Sawan, M. Intracortical microstimulation parameters dictate the amplitude and latency of evoked responses. *Brain Stimul.* **9**, 276–284 (2016).
45. Wang, W. H. et al. Piezotronic effect for in situ electrostimulation of neural stem cell therapy for nerve injury. *Nano Energy* **120**, 109181 (2024).
46. Guo, R. et al. 2D Ti(3)C(2)T(x)MXene couples electrical stimulation to promote proliferation and neural differentiation of neural stem cells. *Acta Biomater.* **139**, 105–117 (2022).
47. Adkins, D. L., Hsu, J. E. & Jones, T. A. Motor cortical stimulation promotes synaptic plasticity and behavioral improvements following sensorimotor cortex lesions. *Exp. Neurol.* **212**, 14–28 (2008).
48. Baba, T. et al. Electrical stimulation of the cerebral cortex exerts antiapoptotic, angiogenic, and anti-inflammatory effects in ischemic stroke rats through phosphoinositide 3-kinase/Akt signaling pathway. *Stroke* **40**, e598–e605 (2009).
49. Yang, K. et al. Electroconductive nanoscale topography for enhanced neuronal differentiation and electrophysiological maturation of human neural stem cells. *Nanoscale* **9**, 18737–18752 (2017).
50. Michelson, N. J., Eles, J. R., Vazquez, A. L., Ludwig, K. A. & Kozai, T. D. Y. Calcium activation of cortical neurons by continuous electrical stimulation: Frequency dependence, temporal fidelity, and activation density. *J. Neurosci. Res.* **97**, 620–638 (2019).
51. Wang, Z., Feng, Z. & Wei, X. Axonal stimulations with a higher frequency generate more randomness in neuronal firing rather than increase firing rates in rat hippocampus. *Front Neurosci.* **12**, 783 (2018).
52. Lea-Carnall, C. A., Trujillo-Barreto, N. J., Montemurro, M. A., El-Deredy, W. & Parkes, L. M. Evidence for frequency-dependent cortical plasticity in the human brain. *Proc. Natl. Acad. Sci. USA* **114**, 8871–8876 (2017).
53. Xu, C., Zhao, M. X., Poo, M. M. & Zhang, X. H. GABA(B) receptor activation mediates frequency-dependent plasticity of developing GABAergic synapses. *Nat. Neurosci.* **11**, 1410–1418 (2008).
54. Tan, L. L. et al. Gamma oscillations in somatosensory cortex recruit prefrontal and descending serotonergic pathways in aversion and nociception. *Nat. Commun.* **10**, 983 (2019).
55. Wang, Y., Yang, X., Zhang, X., Wang, Y. & Pei, W. Implantable intracortical microelectrodes: reviewing the present with a focus on the future. *Microsyst. Nanoeng.* **9**, 7 (2023).
56. Musk, E. An integrated brain-machine interface platform with thousands of channels. *J. Med. Internet Res.* **21**, e16194 (2019).
57. Roy, N. S. et al. Functional engraftment of human ES cell-derived dopaminergic neurons enriched by coculture with telomerase-immortalized midbrain astrocytes. *Nat. Med.* **12**, 1259–1268 (2006).
58. Cao, C. et al. Cholesterol-induced LRP3 downregulation promotes cartilage degeneration in osteoarthritis by targeting Syndecan-4. *Nat. Commun.* **13**, 7139 (2022).

Acknowledgements

This work was supported by the National Key Research and Development Program of China (2021YFF1200800), the National Natural Science Foundation of China (82171861, 82101853, 82101448).

Author contributions

N.H., X.H.L., and D.M. were responsible for study conception and design. N.H., J.X.S., P.F.H., and C.C. performed experiments. N.H., J.X.S., X.H.L.,

H.H.X., W.W.S., Z.H.C., and D.G. contributed to data analysis and interpretation. Z.H.C., X.F., N.H., and D.G. contributed to the organoid culture and transplantation. J.X.S., Z.H.C., P.F.H. and X.W.Z. contributed to surgical implantation of flexible electrode, daily stimulation based on the OBCIs and behavior test. N.H., J.C.Z., C.C., and Z.H.C. conducted and analyzed immunofluorescence. N.H., X.H.L., W.W.S., and C.C. contributed to immunostaining data interpretation. J.X.S., P.F.H., H.H.X. and X.W.Z. analyzed electrophysiological data and behavioral data. N.H., X.H.L., D.M., and J.X.S. contributed to functional data interpretation. N.H., X.H.L., J.X.S., and C.C. prepared figures and drafted the manuscript. N.H., X.H.L., J.X.S., Z.H.C., H.H.X., P.F.H., and D.M. revised the manuscript. All authors approved the final version of the manuscript.

Competing interests
The authors declare no competing interests.

Ethics approval
All animal procedures involving animals were conducted in accordance with the approved protocol for the care and use of laboratory animals by the Animal Care Committee of Tianjin University (Ethical approval number: 23658/42, Animal license number: SYXK (Jin) 2021-0003). All the authors compliance with all relevant ethical regulations.

Additional information
Supplementary information The online version contains supplementary material available at https://doi.org/10.1038/s41467-024-53858-2.

Correspondence and requests for materials should be addressed to Xiao-Hong Li.

Peer review information *Nature Communications* thanks the anonymous reviewers for their contribution to the peer review of this work. A peer review file is available.

Reprints and permissions information is available at http://www.nature.com/reprints

Publisher's note Springer Nature remains neutral with regard to jurisdictional claims in published maps and institutional affiliations.

Open Access This article is licensed under a Creative Commons Attribution-NonCommercial-NoDerivatives 4.0 International License, which permits any non-commercial use, sharing, distribution and reproduction in any medium or format, as long as you give appropriate credit to the original author(s) and the source, provide a link to the Creative Commons licence, and indicate if you modified the licensed material. You do not have permission under this licence to share adapted material derived from this article or parts of it. The images or other third party material in this article are included in the article's Creative Commons licence, unless indicated otherwise in a credit line to the material. If material is not included in the article's Creative Commons licence and your intended use is not permitted by statutory regulation or exceeds the permitted use, you will need to obtain permission directly from the copyright holder. To view a copy of this licence, visit http://creativecommons.org/licenses/by-nc-nd/4.0/.

© The Author(s) 2024